

1 Seismic data analysis for subglacial lake D2 beneath David Glacier, 2 Antarctica

3 Hyeontae Ju^{1,2}, Seung-Goo Kang³, Yeonjin Choi³, Sukjoon Pyun², Min Je Lee³, Hoje Kwak⁴, Kwansoo
4 Kim¹, Yeadong Kim⁵, Jong Ik Lee³

5 ¹Center of Technology Development, Korea Polar Research Institute, Incheon 21990, Korea

6 ²Department of Energy Resource Engineering, Inha University, Incheon 22212, Korea

7 ³Division of Glacier & Earth Sciences, Korea Polar Research Institute, Incheon 21990, Korea

8 ⁴Unit of Antarctic Inland Research, Korea Polar Research Institute, Incheon 21990, Korea

9 ⁵Korea National Committee on Polar Research, Incheon 21990, Korea

10

11 *Correspondence to:* Seung-Goo Kang (ksg9322@kopri.re.kr)

12 **Abstract.** Subglacial lakes beneath Antarctic glaciers are pivotal in advancing our understanding of cryosphere dynamics,
13 basal hydrology, and microbial ecosystems. We investigate the internal structure and physical properties of Subglacial Lake
14 D2 (SLD2), which is located beneath David Glacier in East Antarctica, using seismic data acquired during the 2021/22 austral
15 summer. The dataset underwent a comprehensive processing workflow, including noise attenuation, velocity analysis, and
16 prestack time migration. The migrated seismic sections revealed distinct reverse- and normal-polarity reflections at the glacier–
17 lake and lake–bed interfaces, respectively. We compared the synthetic seismogram generated through wave propagation
18 modeling on the basis of our structural interpretation of the migrated sections with the field data to validate the subglacial lake
19 structure inferred from the seismic data. This confirmed that the water column thickness ranged from approximately 53 to 82
20 m and delineated the broader structure of the subglacial lake. Additionally, discontinuous reflections detected in seismic
21 sections transverse to the ice flow were interpreted as scour-like feature surfaces formed by ice movement. A comparison with
22 airborne ice-penetrating radar (IPR) data acquired in 2018 further supported the consistency of the ice thickness estimates.
23 Notably, a steeply dipping bedrock boundary identified along profile 21YY provided a more precise definition of the lateral
24 extent of SLD2 than was possible when IPR data alone were used. Collectively, these findings enhance our understanding of
25 subglacial lake environments and inform the selection of future drilling sites for in situ sampling.

26 1 Introduction

27 Subglacial lakes beneath the Antarctic ice sheet are typically overlain by glaciers several kilometers thick and have remained
28 isolated from direct atmospheric and solar influences for millions of years, creating extreme environments characterized by
29 low temperatures (Thoma et al., 2010) and high pressures (Tulaczyk et al., 2014). With increasing scientific interest, subglacial
30 lakes have become a focal point for studies related to the Antarctic paleoclimate, as inferred from lake sediments, as well as
31 investigations into microbial life in polar ecosystems (Bell et al., 2007, 2011; Bentley et al., 2009; Christner et al., 2014;

32 Engelhardt et al., 1990; Priscu and Christner, 2003; Rose, 1979; Wingham et al., 2006). Subglacial lakes in Antarctica are
33 generally categorized as either stable or active. Approximately 80% of subglacial lakes in Antarctica are classified as stable
34 subglacial lakes. These closed systems do not exhibit significant surface elevation changes and where subglacial water remains
35 largely isolated, with minimal exchange due to slow and stable recharge and discharge cycles. The remaining 20% are
36 classified as active subglacial lakes, which exhibit surface elevation changes due to episodic water drainage and refilling events
37 (Livingstone et al., 2022). Such active lakes can reduce basal friction as they expand, thereby facilitating glacier flow and, in
38 some cases, accelerating calving processes, ultimately influencing glacier dynamics (Bell et al., 2007; Stearns et al., 2008;
39 Winsborrow et al., 2010). Characterizing subglacial lakes is essential for understanding cryospheric processes, reconstructing
40 past climate conditions, and assessing the potential for life in isolated, extreme environments.

41 The sampling of subglacial lake water, sediments, and microbial communities is critical to address these scientific objectives.
42 However, successful sampling requires careful selection and characterization of the drilling site. Airborne ice-penetrating radar
43 (IPR) surveys are commonly employed at regional scales to detect potential subglacial lakes suitable for drilling (Christianson
44 et al., 2012; Lindzey et al., 2020; Yan et al., 2022). However, due to signal attenuation in water, IPR surveys are limited in
45 resolving the internal structure of subglacial lakes. To overcome this limitation, seismic surveys have been conducted at
46 potential subglacial lake candidates identified from IPR surveys. During such surveys, P-waves propagate through the water
47 column and are partially reflected at the lake–bed interface because of contrasts in acoustic impedance. Analyzing these
48 reflected waves enables detailed delineation of the water column and underlying substrate, thereby informing optimal drilling
49 locations (Brisbourne et al., 2023; Filina et al., 2008; Horgan et al., 2012; Woodward et al., 2010).

50 As such, numerous studies have utilized seismic surveys to investigate the characteristics of subglacial lakes, including
51 Subglacial Lake Ellsworth, Subglacial Lake Whillans, and Subglacial Lake CECs. Subglacial Lake Ellsworth, located beneath
52 2,930–3,280 m of glacial ice in West Antarctica, was the subject of a seismic survey during the austral summer of 2007–08.
53 This survey revealed spatially variable ice thickness and a lake water column ranging from 52 to 156 m, which guided the
54 identification of an optimal drilling location (Smith et al., 2018; Woodward et al., 2010). Subglacial Lake Whillans lies beneath
55 approximately 800 m of ice. Seismic observations conducted during the 2010/11 field season revealed water columns
56 extending over a 5 km segment of the survey profile, with a maximum thickness of less than 8 m. The glacier bed was
57 predominantly composed of soft sediments, and localized zones with shallow water columns (< 2 m) were also identified
58 (Horgan et al., 2012). Subsequent drilling in the summer of 2012/13 confirmed the presence of microbial life in both the water
59 and sediment samples (Christner et al., 2014). Subglacial Lake CECs (SLCECs), located beneath 2653 m of ice at the Rutford–
60 Institute–Minnesota Divide in West Antarctica, were investigated through seismic surveys conducted in the 2016/17 and
61 2021/22 seasons. These surveys revealed a maximum water column thickness of 301.3 ± 1.5 m and clastic sediments up to 15
62 m thick covering the lakebed. While the lake center was relatively flat, significant topographic variability was observed near
63 the lake margins (Brisbourne et al., 2023).

64 We have initiated subglacial lake research beneath David Glacier, the closest major glacier to Jang Bogo Station in East
65 Antarctica. Satellite altimetry has identified six subglacial lakes in this region (Smith et al., 2009; Wright and Siegert, 2012).

66 During the 2016/17 austral summer, an airborne IPR survey was conducted over the region encompassing Subglacial Lake D1
67 (SLD1) and Subglacial Lake D2 (SLD2) (Lindzey et al., 2020). A subsequent high-resolution IPR survey was carried out
68 during the 2018/19 field season, focusing solely on SLD2 (Ju et al., 2025). The combined results of the two surveys revealed
69 moderately enhanced radar bed echoes relative to the surrounding area, specularity values (>0.4), a depressed basal elevation
70 (≤ -350 m), and a low hydraulic gradient ($\leq 0.84^\circ$), collectively indicating high potential for the presence of subglacial water
71 beneath SLD2. Building upon these observations, Ju et al. (2025) subdivided the previously identified single subglacial water
72 body at SLD2, as detected by ICESat altimetry, into three smaller subglacial lakes: SLD2-A, SLD2-B, and SLD2-C. Among
73 these, SLD2-A represents the largest areal extent, and targeted seismic surveys were conducted over this area to obtain high-
74 resolution information on the lake depth and basal structure. In the 2019/20 season, an initial seismic campaign identified the
75 glacier thickness and suggested the presence of the lake; however, the data quality was compromised by surface crevasse noise
76 and a lack of adequate fold coverage, limiting detailed interpretation. A refined seismic survey with 8-fold coverage was
77 conducted during the 2021/22 season to address these issues.

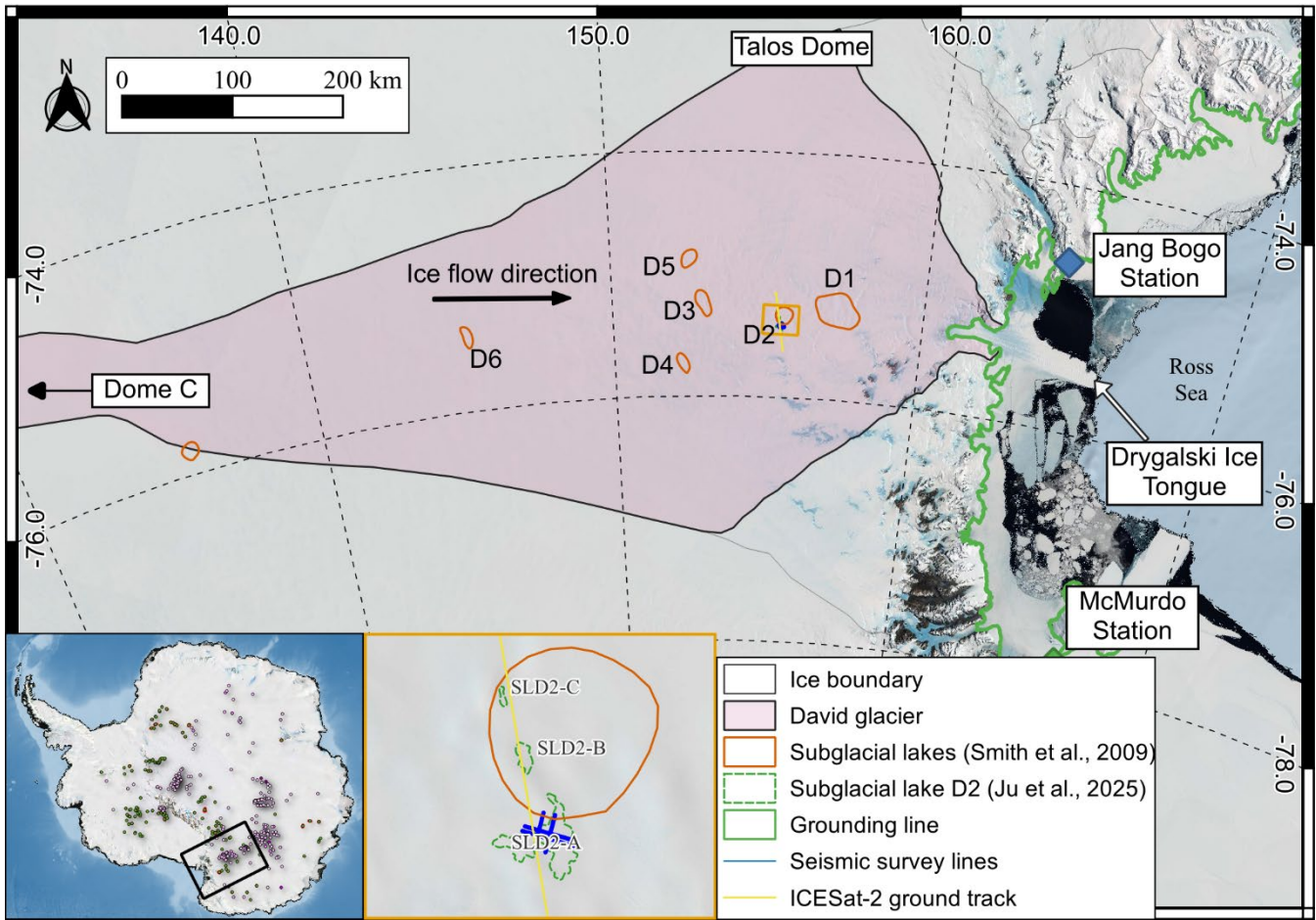
78 In this study, we present a detailed analysis of the physical and structural properties of SLD2-A using seismic data acquired
79 during the 2021/22 campaign. We first describe the seismic data processing workflow, including noise attenuation, amplitude
80 correction, and prestack time migration. The final results reveal seismic reflections corresponding to the glacier–lake and lake–
81 bed interfaces. The seismic interpretation is subsequently validated through a comparison with synthetic seismograms, and a
82 quantitative analysis is performed to determine the key structural characteristics of SLD2-A, including the ice thickness, water
83 column thickness, and basal structure of the lake.

84 **2 Subglacial Lake D2 Beneath David Glacier in Antarctica**

85 **2.1 David Glacier**

86 David Glacier, located in Victoria Land, East Antarctica, originates from the Dome C and Talos Dome regions and flows
87 seaward through the Drygalski Ice Tongue (Fig. 1). The mass balance of glaciers from 1979 to 2008 has been estimated at 7.5
88 ± 0.4 Gt yr $^{-1}$ (Rignot et al., 2019), while the mean ice discharge over the more extended period from 1979 to 2017 was reported
89 to be approximately 9.7 Gt yr $^{-1}$ (Frezzotti et al., 2000; Rignot et al., 2019). According to Smith et al. (2020), satellite altimetry
90 observations from ICESat-1 and ICESat-2 (2003–2019) indicate that the grounded portion of David Glacier experienced a mass
91 gain of 3 ± 2 Gt yr $^{-1}$, whereas the adjacent ice shelves exhibited a mass loss of -1.6 ± 1 Gt yr $^{-1}$. Although the overall mass
92 balance of David Glacier currently appears stable, it remains uncertain how long this stability can be maintained.

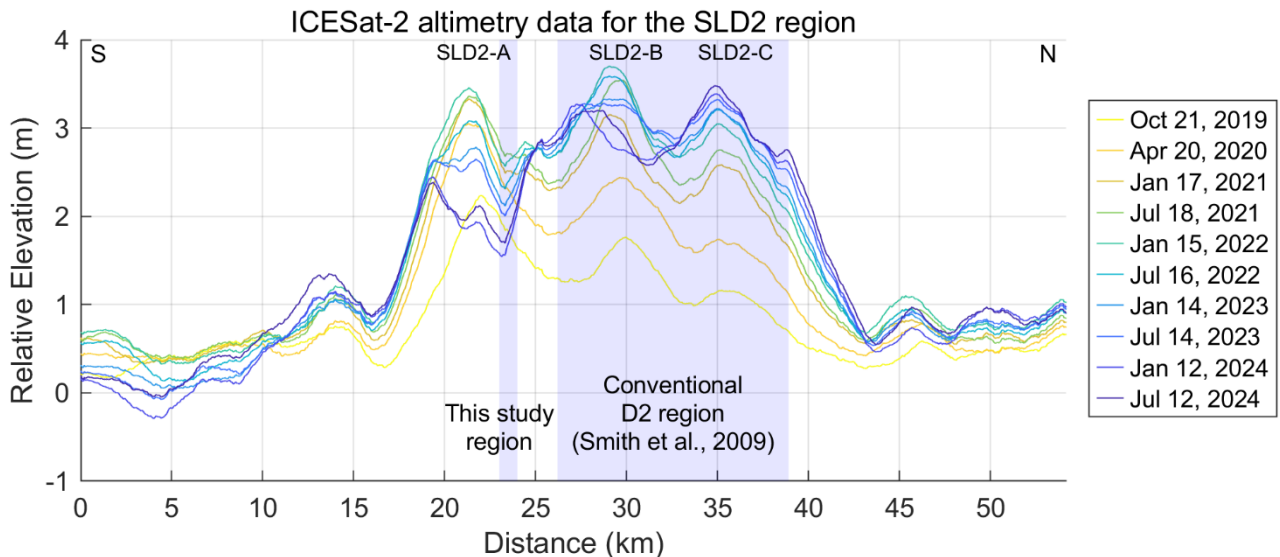
93



94
95 **Figure 1: Locations of subglacial lakes D1–D6 in the David Glacier region, Victoria Land, Antarctica (EPSG: 4326–WGS84).**
96

97 2.2 Subglacial Lake D2

98 Among the six subglacial lakes (D1–D6) identified beneath David Glacier via satellite altimetry (Smith et al., 2009; Wright
99 and Siegert, 2012), SLD2 was observed to have experienced a drainage event between 2003 and 2008 on the basis of ICESat
100 altimetry data (Smith et al., 2009). Since the drainage event, a continuous increase in surface elevation over SLD2 has been
101 observed, indicating water refilling, as detected from CryoSat-2 altimetry data (2013–2017) (Siegfried and Fricker, 2018) and,
102 more recently, from ICESat-2 observations (2019–2024) (Fig. 2). Figure 2 shows elevation changes relative to April 2019,
103 indicating surface uplift through January 2022. After this period, the surface elevation remained stable in the region originally
104 delineated as SLD2 by Smith et al. (2009), whereas a decreasing elevation trend was observed in the SLD2-A region (Ju et al.,
105 2025). These patterns of elevation change strongly suggest that SLD2 is an active subglacial lake, with cyclic drainage and
106 refilling likely contributing to the presence of subglacial sediments.



109 **Figure 2: Glacier surface elevation changes derived from ICESat-2 altimetry between 22 April 2019 and 12 July 2024.** The X-axis
110 corresponds to the 22 April 2019 dataset, and all subsequent elevation changes are referenced to this date. The light blue shaded
111 region indicates the spatial overlap between the conventional SLD2 region identified by Smith et al. (2009) and our study region.

113 To better constrain the lake's extent and basal conditions of SLD2, airborne IPR survey data from 2016/17 (Lindzey et al.,
114 2020) and 2018/19 (Ju et al., 2025) field campaigns indicate that glacier surface elevations in the SLD2 region range from
115 approximately 1820 to 1940 m, with ice thicknesses varying between 1685 and 2293 m. Furthermore, the observations of
116 moderately enhanced radar bed echoes relative to the surrounding area, elevated specularity values (>0.4), depressed basal
117 elevations (≤-350 m), the presence of a Bain-like topography, a lower hydraulic head than the surroundings, and low hydraulic
118 gradients ($\leq 0.84^\circ$) collectively suggest a high potential for the presence of subglacial water beneath SLD2. (Ju et al., 2025;
119 Lindzey et al., 2020).

120 3 Method

121 3.1 Seismic survey

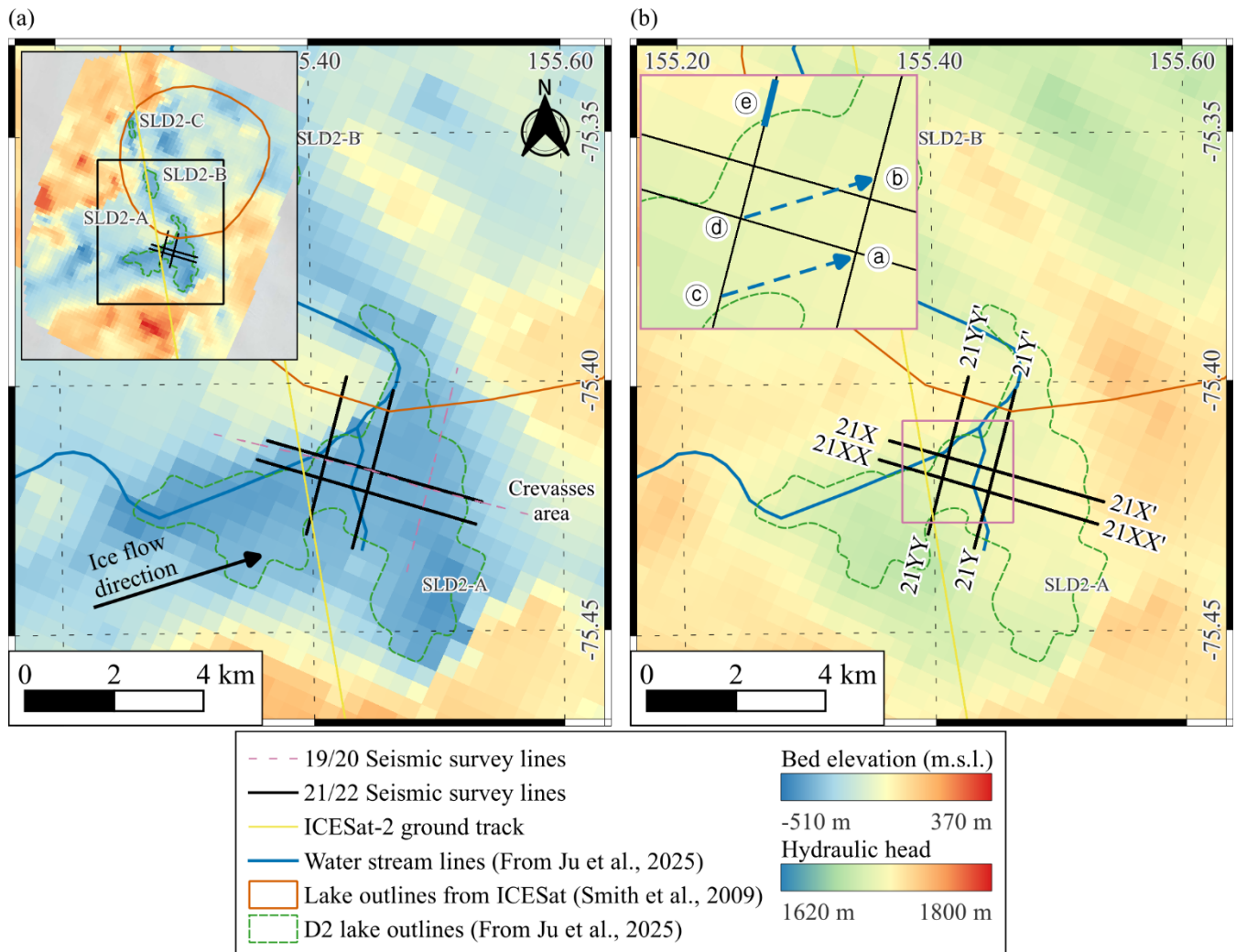
122 As previously noted, the internal structure and water column of subglacial lakes cannot be fully resolved using IPR alone
123 because of signal attenuation in water. Accordingly, a seismic survey was conducted within the candidate SLD2-A region
124 identified from IPR data to investigate the structure of the subglacial lake more precisely.

125 During the 2019/20 austral summer, a preliminary seismic survey was conducted over the SLD2-A region to evaluate the
126 potential presence of a subglacial lake and to obtain initial information on its structural characteristics. Owing to limited field
127 time and equipment constraints, the fold of coverage for all survey lines was restricted to 1, and all shot points were aligned

128 near surface crevasses. Consequently, the acquired seismic data were significantly contaminated by strong linear coherent
129 noise associated with crevasses, which severely degraded the signal quality of key reflectors, particularly reflections from the
130 subglacial lake–bedrock interface. In addition, explosives are deployed within shallow boreholes (< 20 m depth), and owing
131 to the absence of proper backfilling and the rapid timing of detonation, poor coupling between the explosives and the borehole
132 walls further reduces energy transmission efficiency, resulting in overall low-quality reflection signals (Ju et al., 2024). As a
133 result, due to the limitations of single-fold acquisition, stacking was not feasible, resulting in a low signal-to-noise ratio (SNR)
134 and the presence of dominant coherent noise, rendering the seismic dataset unsuitable for quantitative structural interpretation.
135 Nevertheless, the preliminary survey qualitatively confirmed the glacier thickness beneath SLD2-A and suggested the presence
136 of subglacial water, providing critical baseline information that guided the methodology and survey design of the subsequent
137 detailed seismic campaign conducted during the 2021/22 season.

138 For the refined survey, seismic acquisition lines were planned using bed topography derived from the IPR and surface elevation
139 data from satellite altimetry. A total of four seismic lines were acquired and designated 21X, 21Y, 21XX, and 21YY (Fig. 3).
140 Lines 21X and 21XX, oriented approximately 52° relative to the ice flow direction, are situated at an average surface elevation
141 of 1894 ± 13 m. Lines 21Y and 21YY, oriented approximately -30° in the ice flow direction, lie at an average elevation of
142 1887 ± 16 m. All lines traverse regions of minimal topographic relief, with average surface slopes of approximately 0.5°,
143 indicating a relatively flat and stable glacier surface. The lengths of the 21X/21XX and 21Y/21YY lines are approximately 5
144 km and 3.5 km, respectively. Seismic acquisition for lines 21X and 21Y was conducted using 8-fold coverage to increase the
145 resolution, whereas lines 21XX and 21YY were acquired with 4-fold coverage due to time constraints during the survey. The
146 additional acquisition parameters are summarized in Table 1.

147



148

149 **Figure 3: 21/22 seismic survey layout (black lines) overlaid on (a) bed elevation and (b) hydraulic head data from IPR results (Ju et**

150 al., 2025).

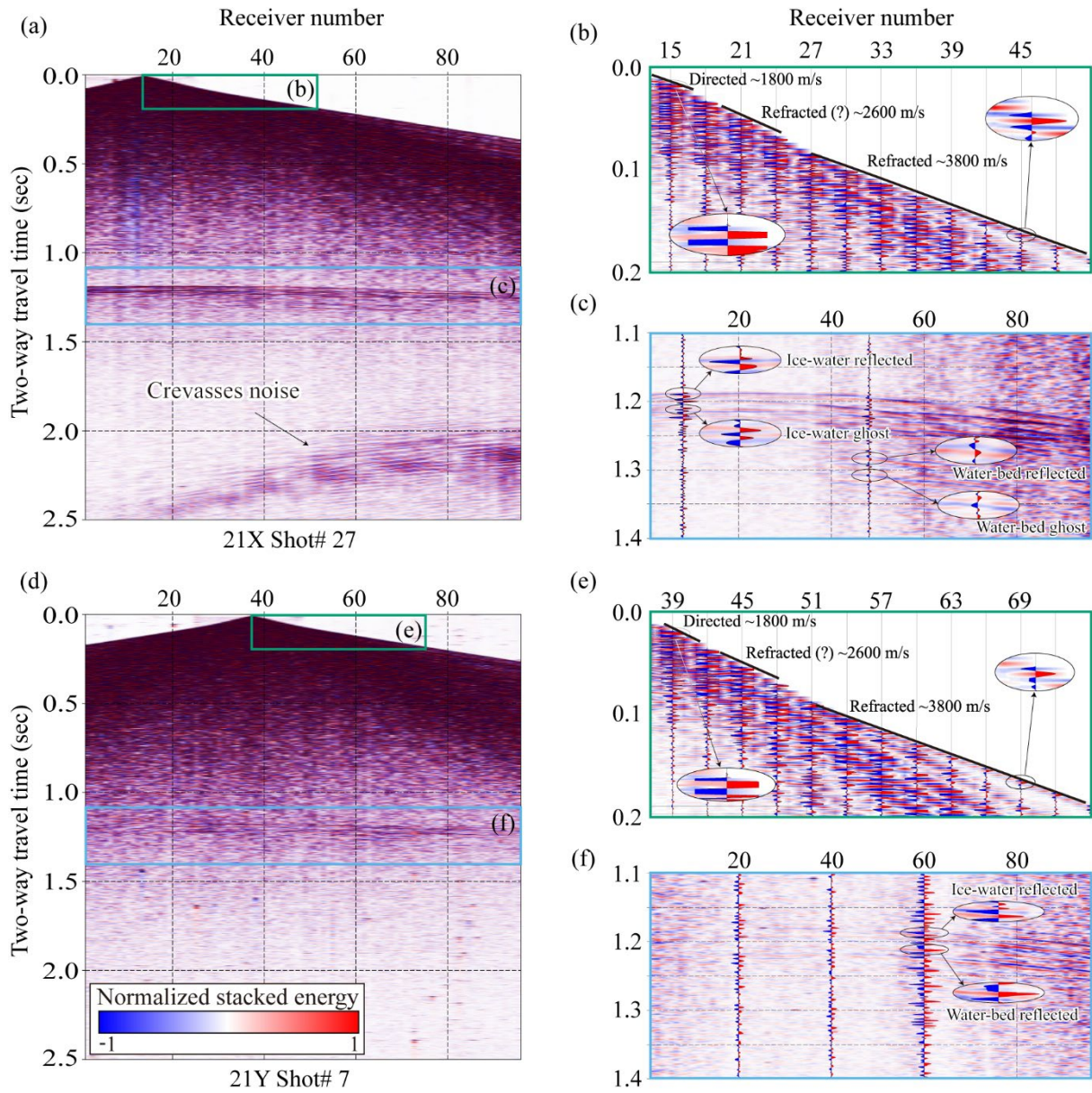
151

152 **Table 1: Parameters of the active-source seismic survey.**

Survey Parameters	Survey lines			
	21X line	21Y line	21XX line	21YY line
Line length (km)	5	3.5	5	3.5
Fold	8	8	4	4
Shot interval (m)	90	90	180	180
Number of shots	56	40	28	20
Receiver channels		96		
Receiver interval (m)		15		
Recording time (s)		4		
Record peak frequency (kHz)		1		
Record sampling rate (ms)		0.25		
Survey time (days)		34		
Survey crew size	Hot water drilling (3), Seismic (6)			

153

154 Before the seismic survey, a ground-penetrating radar (GPR) survey was used to identify the firn transition zone at depths of
 155 approximately 20–22 m. To enhance seismic signal transmission, 1.6 kg of pentaerythritol tetranitrate (PETN) explosives were
 156 emplaced at depths of 25–30 m using hot water drilling techniques. A total of 144 shots were deployed across the four survey
 157 lines. Given the snow-covered glacier surface, Georods were used instead of conventional spike-type geophones to increase
 158 signal detection efficiency (Voigt et al., 2013). Each Georod houses four geophone elements in a 0.6 m-long cylindrical array,
 159 producing a single output by summing the inputs from all the elements. Compared with traditional geophones, this
 160 configuration improves coupling and detection performance in snow-dominated environments (Ju et al., 2024). Figure 4
 161 presents shot gather #27 from line 21X and shot gather #7 from line 21Y. In these shot gathers, the velocity of the direct wave
 162 is estimated to be approximately 1800 m/s, and the refracted wave velocity is approximately 3800 m/s. First-arrival analysis
 163 of the direct wave indicates a normal polarity, confirming the source waveform polarity. A prominent negative polarity
 164 reflection is observed at a two-way travel time (TWT) of approximately 1.2 s, interpreted as the glacier–lake interface.
 165 Approximately 25–30 ms later, a ghost reflection with normal polarity appears. A subsequent reflection at approximately 1.3 s
 166 TWT, showing normal polarity, is attributed to the lake–bed interface, followed by its negative polarity ghost reflection 25–
 167 30 ms later. In shot gather #27, noise originating from crevasses becomes apparent from approximately 2 s TWT. As the
 168 distance to the crevasses decreases, this noise increasingly overlaps with the primary reflection arrivals, complicating the
 169 interpretation.



170

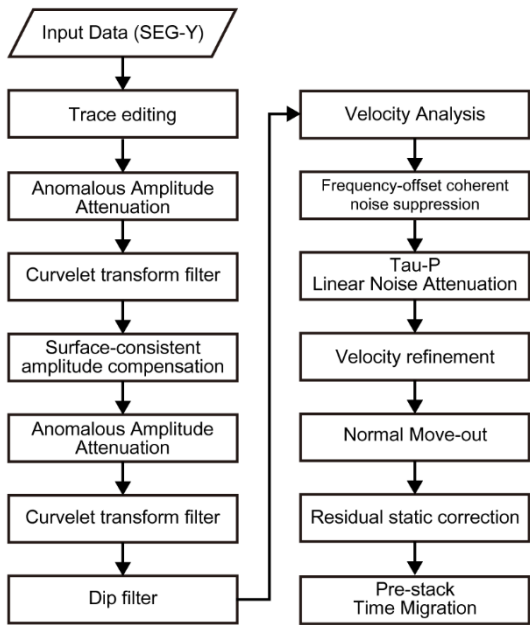
171 **Figure 4: Raw shot records from seismic lines 21X (a) and 21Y (d). Panels (b) and (e) are zoomed-in views of the early arrival window**
172 **(0.0–0.2 s) from panels (a) and (d), respectively, used to calculate the apparent velocities of the direct and refracted waves. These**
173 **panels highlight that the first arrivals of both the direct wave (clipped for display) and the refracted wave exhibit positive polarity.**
174 **The direct wave, propagating through the upper firn layer (0–25 m depth), shows an apparent velocity of approximately 1800 m/s,**
175 **while the refracted wave traveling through glacier ice has an apparent velocity of approximately 3800 m/s. Panels (c) and (f) are**
176 **zoomed-in views of the deeper arrivals (1.1–1.4 s) from panels (a) and (d), respectively. Reflections from the ice–water interface**
177 **exhibit negative polarity, whereas those from the water–bed interface display positive polarity.**

178

179 **3.2 Seismic data processing**

180 Although seismic data acquired from glaciers share processing similarities with those of land-based surveys, glaciological
 181 factors, such as surface cracks, crevasses, and strong winds, introduce substantial noise that can degrade data quality (Johansen
 182 et al., 2011; Zechmann et al., 2018). Among these factors, linear noise generated by crevasses is particularly detrimental, often
 183 obscuring key reflections (Dow et al., 2013). Hence, the glacier seismic data underwent multiple data processing sequences
 184 focused on linear noise removal (Fig. 5). Acquisition geometry was added to the data using the raw data and geometry
 185 information. Multiple data processing and noise removal processes were then carried out to increase the signal-to-noise ratio
 186 (SNR).

187



188 **Figure 5: Schematic of the seismic data processing workflow based on the Omega geophysical data processing platform (SLB),**
 189 **including noise attenuation, amplitude correction, velocity analysis, and prestack time migration.**

191

192 The initial processing involved anomalous amplitude attenuation (AAA), implemented via a spatial median filter. This step
 193 targets outlier amplitudes within a defined frequency band, attenuating anomalous signals through interpolation across
 194 neighboring traces. A curvelet transform-based filter was subsequently applied to remove coherent noise. Curvelet
 195 decomposition enables the separation of signals on the basis of dip angle and scale, allowing for the selective removal of
 196 ground roll and other coherent noise components that differ in dip from true reflections (Oliveira et al., 2012). In this study,
 197 linear coherent noise at later arrival times (>2.0 s) was effectively removed using this method.
 198 Surface-consistent amplitude compensation (SCAR) and surface-consistent deconvolution were employed to normalize the
 199 amplitude variability across shot gathers. These steps were followed by a second round of AAA and curvelet filtering to

200 suppress artifacts introduced during the compensation and deconvolution stages. Dip filtering was also applied to eliminate
201 spurious hyperbolic arrivals, which were manually identified and removed.

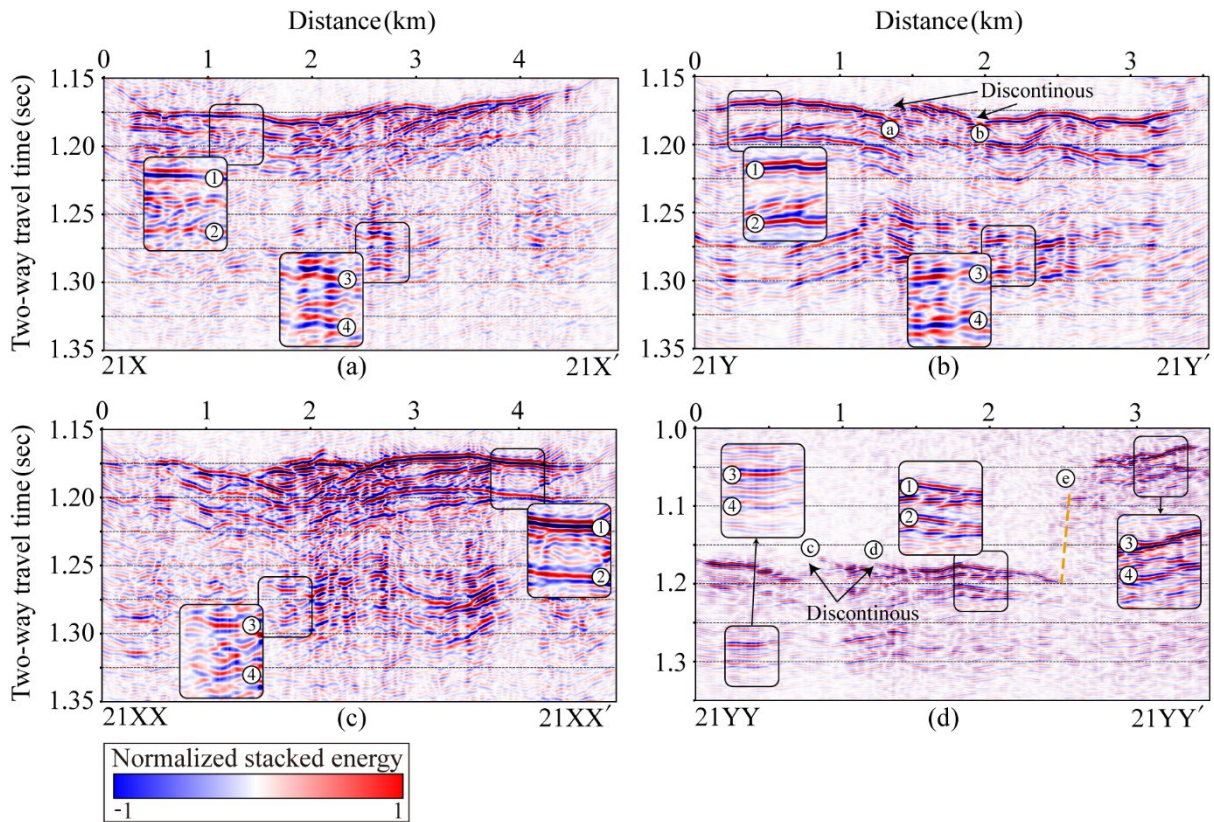
202 Velocity analysis was conducted at intervals of 40 common midpoints to construct a migration velocity model. Frequency–
203 offset coherent noise suppression (FXCNS) was used to attenuate linear-related noise, followed by Tau-p linear noise
204 attenuation (LNA), effectively reducing the noise associated with crevasse scattering. The final processing steps included
205 velocity model refinement, normal move-out (NMO) correction, and prestack time migration (PSTM). The specific parameters
206 employed for data processing, as well as the intermediate outcomes at each processing stage, are provided in the supplementary
207 information (S1).

208 To increase imaging accuracy, a residual static correction was applied before migration using glacier surface elevation data.
209 The final migrated seismic section was produced using Kirchhoff PSTM. The migrated data have a center frequency of
210 approximately 180 Hz. Assuming seismic wave velocities between 1395 m/s and 3800 m/s, the corresponding vertical
211 resolutions, which are calculated using the quarter-wavelength criterion, range from approximately 2.01 m to 5.27 m. This
212 resolution is adequate for imaging SLD2.

213 4 Seismic data processing results

214 Figure 6 presents the PSTM results for the four seismic survey lines. On line 21X (Fig. 6a), a strong, laterally continuous
215 reflection with reverse polarity is observed at 0.3–4.8 km along the profile, and the two-way travel time (TWT) is
216 approximately 1.15–1.18 s. This reflection is interpreted as the glacier–lake interface (①). Approximately 25–30 ms below
217 this horizon, a normal-polarity reflection (②) appears, likely representing a ghost signal associated with the primary glacier–
218 lake reflection. A deeper normal-polarity reflection is observed within 1.9–3.1 km at TWTs of 1.25–1.27 s (③), which is
219 interpreted as the lake–bed interface. This is followed by a reverse-polarity reflection 25–30 ms later (④), which is presumed
220 to be the corresponding ghost of the lake–bed interface.

221



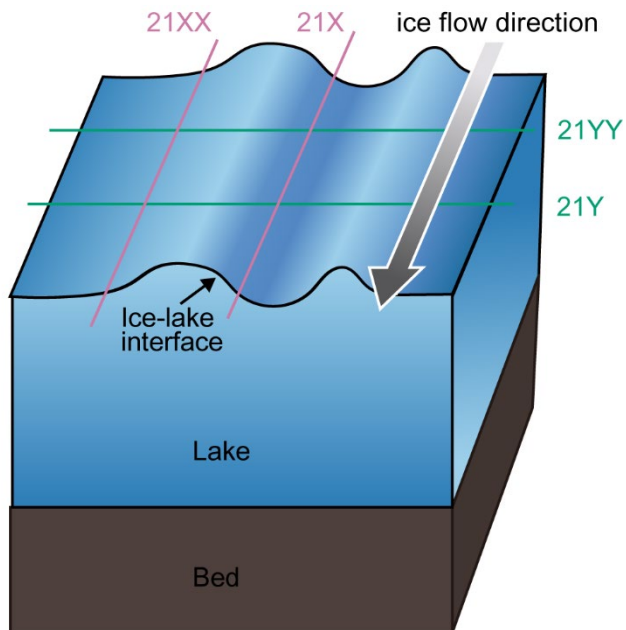
222
223 **Figure 6: PSTM seismic sections for lines (a) 21X, (b) 21Y, (c) 21XX, and (d) 21YY prior to ghost removal. Ghost reflections appear**
224 **25–30 ms beneath the glacier–lake and lake–bed interfaces due to the 25 m source depth.**

225
226 In line 21Y (Fig. 6b), similar features are observed. A reverse-polarity reflection, interpreted as the glacier–lake interface (①),
227 is observed within 0.1–3.2 km at TWT 1.17–1.18 s, with its ghost reflection (②), which exhibits normal polarity and appears
228 25–30 ms later. A normal-polarity reflection within 0.1–3.2 km at a TWT of 1.26–1.27 s is interpreted as the lake–bed interface
229 (③), followed by a reverse-polarity ghost signal (④). Additionally, discontinuous reflections interpreted as subglacial scour-
230 like features (SLF) are visible at approximately 1.3 km (ⓐ) and 1.9 km (ⓑ) along line 21Y at TWT 1.18 s (black arrows in
231 Fig. 6b). These features may be associated with glacial erosion of the underlying substrate.
232 In line 21XX (Fig. 6c), a reverse-polarity reflection, interpreted as the glacier–lake interface (①), is observed within 0–4.3
233 km at a TWT of 1.17–1.18 s. This reflection is followed 25–30 ms later by a normal-polarity reflection (②), which is
234 considered the ghost of the primary glacier–lake interface. Further down the section, a normal-polarity reflection (③) within
235 1.9–4.2 km at a TWT of 1.25–1.28 s is interpreted as the lake–bed interface, followed by its ghost reflection (④) 25–30 ms
236 later.
237 On line 21YY (Fig. 6d), the glacier–lake interface (①) is marked by a strong, flat, reverse-polarity reflection at 0–2.4 km and
238 a TWT of 1.17–1.20 s, followed by its normal-polarity ghost (②) 25–30 ms below. Lake–bed interface reflections (③) are

239 observed within 0.2–2.4 km at TWTs of 1.27–1.29 s, followed by a reverse-polarity ghost (④) 25–30 ms later. Within 2.4–
240 2.55 km and TWTs of 1.08–1.17 s, no coherent reflection is visible due to the steeply dipping bed topography, as indicated by
241 the dashed orange line in Fig. 6d. Within 2.55–3.4 km and a TWT of 1.03–1.09 s, a stair-step-shaped reflection at the glacier–
242 bed interface (③) is identified, followed by its reverse-polarity ghost (④). Additionally, similar to observations on line 21Y,
243 discontinuous reflections interpreted as SLF surfaces appear at 0.7 km (⑤) and 1.2 km (⑥) along line 21YY at TWT 1.18 s
244 (black arrows in Fig. 6d).

245 The discontinuous reflection signals identified on lines 21Y and 21YY are spatially aligned along the ice flow direction when
246 projected laterally (Fig. 3, dashed blue arrow). This alignment suggests that the observed discontinuities correspond to a
247 subglacial SLF surface formed by glacial motion. The SLF is visible predominantly on lines 21Y and 21YY, which are oriented
248 more perpendicularly to the ice flow direction, thereby enhancing the expression of lateral subglacial variability. In contrast,
249 lines 21X and 21XX are more parallel to the ice flow, resulting in a foreshortened view of the subglacial structures and a
250 relatively flat appearance in the seismic sections (Fig. 7).

251



252

253 **Figure 7: Conceptual diagram illustrating the orientation of seismic survey lines relative to subglacial structures and the ice flow**
254 **direction, explaining the appearance of structural features in each line.**

255

256 **5 Comparison between field data and synthetic seismograms**

257 The depth estimation of subsurface structures from PSTM sections is subject to errors arising primarily from inaccuracies or
 258 uncertainties in the seismic velocity model. An inaccurate velocity model may result in erroneous positioning of reflection
 259 events, leading to misinterpretation of stratigraphic horizons (Herron, 2000; Yilmaz, 2001). Such limitations are typically
 260 mitigated through well-tie analysis, wherein seismic horizons are calibrated against borehole data. However, in the case of
 261 SLD2, no borehole data are currently available.

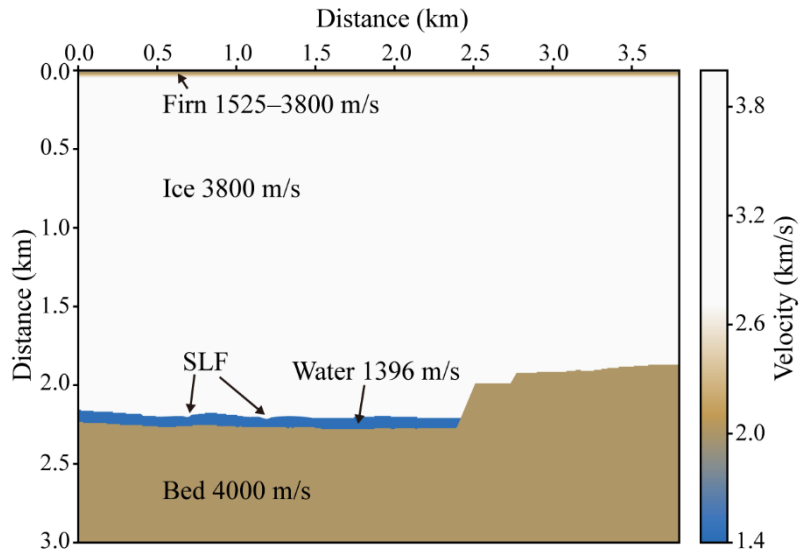
262 We validate the processed field data by performing a comparative analysis with synthetic seismograms to address this
 263 constraint. The forward modeling algorithms based on the staggered grid finite difference method in the time domain were
 264 used (Graves et al., 1996). The velocity model for this seismic modeling is constructed by structural information given by the
 265 seismic migration sections, integrating published values of P-wave velocities for firn, glacial ice, and subglacial water. P-wave
 266 velocities in firn vary from 1525 to 3800 m s⁻¹ because density increases with depth (Kirchner and Bentley, 1979; Picotti et
 267 al., 2015; Qin et al., 2024). Glacial ice has an average P-wave velocity of approximately 3800 ± 5 m s⁻¹ at -2 ± 2 °C (Kohnen,
 268 1974), while subglacial water has a velocity of approximately 1396 ± 2 m s⁻¹ at -1.75 ± 0.25 °C, with a salinity less than 1
 269 PSU (practical salinity units) (Thoma et al., 2010; Tulaczyk et al., 2014). Additionally, on line 21YY, the reflection polarity
 270 at the ice–bedrock interface appears as normal polarity, which indicates an increase in the acoustic impedance. In other words,
 271 this suggests that the P-wave velocity of the bedrock is higher than that of the overlying ice. Therefore, the bedrock P-wave
 272 velocity was set to 4000 m s⁻¹. Using this information, a layered P-wave velocity model comprising firn, glacial ice, subglacial
 273 lakes, and bedrock was developed (Fig. 8). Forward modeling was then conducted using the Ricker wavelet, with acquisition
 274 parameters matching those used in the field survey (Table 2). We applied just the migration step in case of the synthetic dataset,
 275 as it is free of noise.

276

277 **Table 2: Parameters of the synthetic model.**

	Synthetic modeling parameters		
	Thickness (m)	Velocity (m/s)	Density (g/cm ³)
Model size	3.5 km (distance) x 3 km (depth)		
Source	Ricker wavelet (zero-phase), 60 Hz		
Receiver	25 m depth, 90-m interval		
Grid spacing	0 m depth, 15-m interval, 96 channel		
Sampling interval	0.5-m		
Layer parameters	0.1 ms		
Firm	100	1,525–3,800	0.3–0.917
Ice	1,887–2,221	3,800	0.917
Water	0–82±1.3	1,396	1.017
Bed	723–1,113	4,000	2.1

278



279
 280 **Figure 8:** P-wave velocity model used in forward modeling for line 21YY. The upper ~100 m represents firn with velocities ranging
 281 from $1525\text{--}3800\text{ m s}^{-1}$ (Kirchner and Bentley, 1979; Picotti et al., 2015; Qin et al., 2024). The ice below this depth has a velocity of
 282 $3800 \pm 5\text{ m s}^{-1}$ (Kohnen, 1974), and the subglacial water layer has a velocity of $1396 \pm 2\text{ m s}^{-1}$ (Thoma et al., 2010; Tulaczyk et al.,
 283 2014).

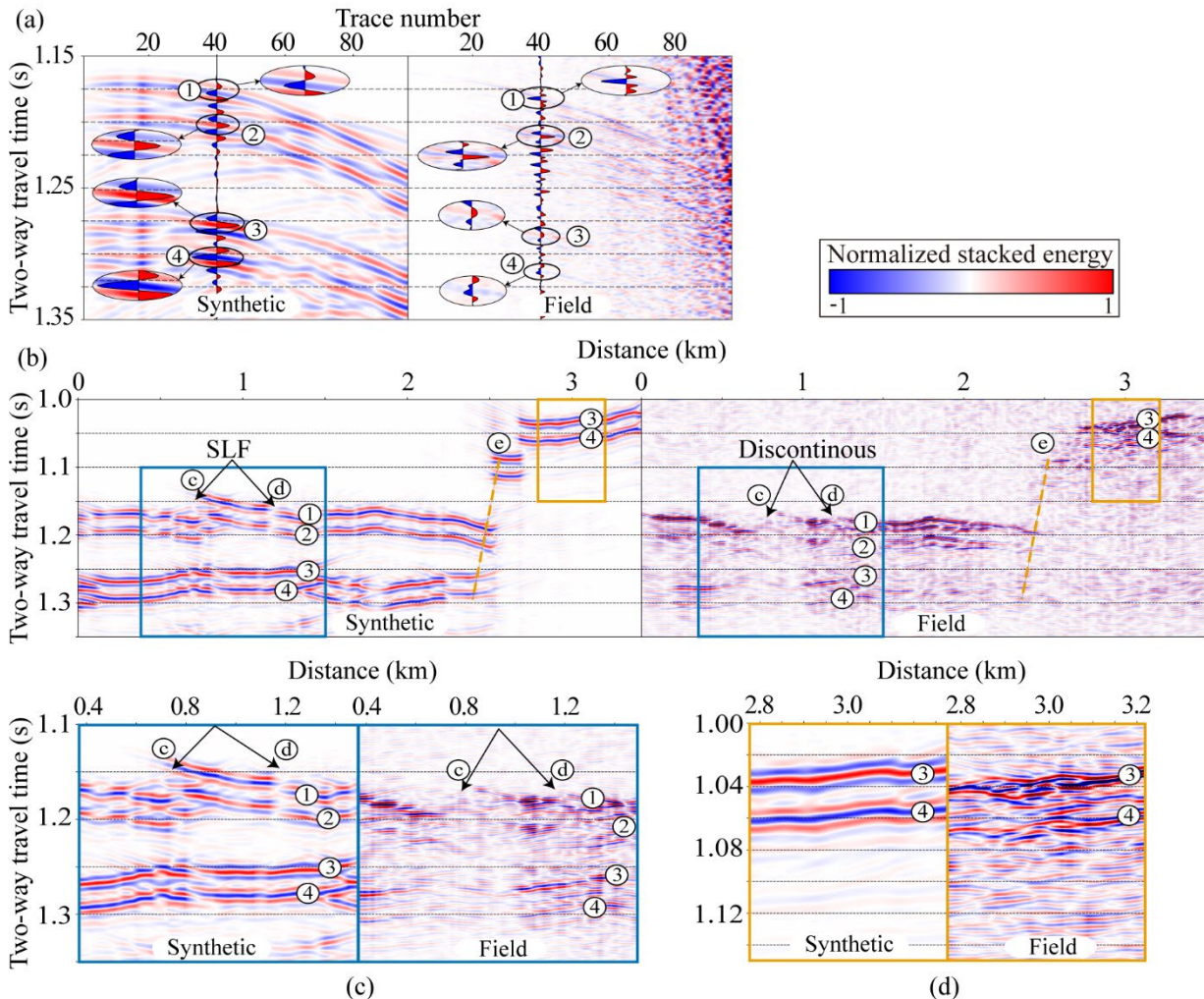
284

285 Figure 9a compares the shot gather from the synthetic dataset (left) and the corresponding gather from seismic data line 21YY
 286 (right) at the same location. A prominent reflection at a TWT of 1.17 s is observed in both datasets, corresponding to the
 287 glacier–lake interface (①). This reflection results in a high impedance contrast and reverse polarity due to the P-wave velocity
 288 difference between glacial ice and water. These features are consistent with previous observations at glacier–lake interfaces
 289 (Atre and Bentley, 1993; Brisbourne et al., 2023; Horgan et al., 2012; King et al., 2004; Peters et al., 2007; Woodward et al.,
 290 2010). A secondary reflection with normal polarity appears approximately 28 ms after the primary event (②) and is interpreted
 291 as a surface ghost reflection. This time delay corresponds to a seismic source depth of approximately 25 m, which is consistent
 292 with previous seismic analyses (Brisbourne et al., 2023; Schlegel et al., 2024). That is, assuming an average P-wave velocity
 293 of 1800 m s^{-1} within the top 25 m, the TWT of the ghost reflection matches the expected delay:

294

$$\text{TWT}_{\text{ghost}} = \frac{2 \times 25\text{ m}}{1800\text{ m/s}} \approx 28\text{ ms.}$$

295



296

297 **Figure 9: Comparison of synthetic and field seismic data.** (a) Shot gather at the same location for synthetic (left) and 21YY field data (right).
298 (b) PSTM images comparison between the synthetic model and the 21YY line.
299 (c) Enlarged views of discontinuous reflections (synthetic, field). (d) Comparison of dipping bed reflections (synthetic, field), showing shadow zones and steep basal topography.

300

301 Furthermore, considering that the acoustic impedance of air is approximately zero ($Z_{air} \approx 0$) and that of ice is Z_{ice} , the
302 reflection coefficient (RC) for an upgoing wave at the air–ice interface can be approximated as follows:

$$303 RC = \frac{Z_{air} - Z_{ice}}{Z_{ice} + Z_{air}} \approx -1. \quad (1)$$

304 This implies that the polarity of the ghost reflection at the surface is reversed relative to the downgoing primary wave (Krail
305 and Shin, 1990; Robinson and Treitel, 2008).

306 Figure 9b compares the PSTM sections of the synthetic model (left) and the field data from line 21YY (right). Unlike the field
307 data, the synthetic dataset is free from ambient noise and features a precise source–receiver geometry, resulting in clearer

308 delineation of subsurface reflections and facilitating structural interpretation. The synthetic and field PSTM sections exhibit
309 four principal reflection events (①–④) at identical TWTs. Reflections ① and ④ are characterized by reverse polarity,
310 whereas ② and ③ display normal polarity, which is consistent across both datasets. Discontinuous reflections observed in
311 the synthetic model are interpreted as indicative of a subglacial SLF surface.

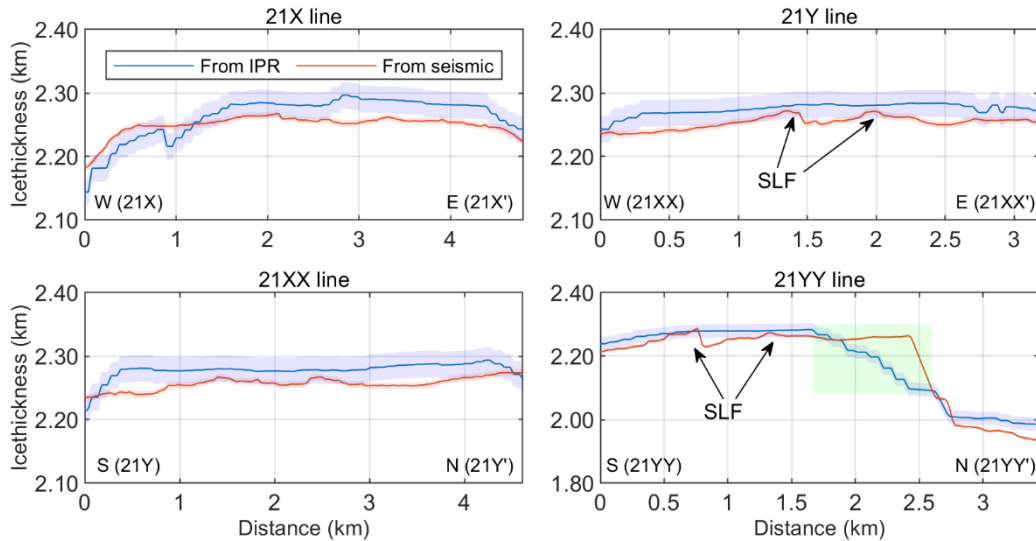
312 Figure 9c provides a magnified comparison of regions synthetic and field, with a focus on discontinuous features. Although
313 the discontinuous reflections and associated low impedance at 0.7 km and 1.2 km (TWT = 1.18 s) in the field data are
314 challenging to resolve, the SLF surface beneath the glacier is imaged in the synthetic section.

315 Figure 9d presents a magnified comparison of regions synthetic and field to examine reflections from a dipping bed. Within
316 2.4–2.55 km and TWTs of 1.08–1.17 s, reflections are temporally dispersed, resulting in a shadow zone where coherent signals
317 are absent. From 0.2–2.4 km, a reversed-polarity reflection (①) is observed, whereas from 2.55–3.4 km, a normal-polarity
318 reflection (③) is present. The latter is interpreted as the glacier–bed interface. The dashed line traces the steeply dipping bed
319 geometry, delineating the lake margin, with an estimated dip angle of approximately 52°. The resulting shadow zone is likely
320 caused by the lateral scattering of seismic energy along the steep slope. The comparison of synthetic PSTM sections confirms
321 that the velocity model used for seismic imaging appropriately represents the structures of glacial and subglacial lakes.

322 To further validate the interpretation, ice thickness estimates from the seismic data were compared with those derived from
323 airborne IPR surveys along four seismic lines (Fig. 10) (Ju et al., 2025). Given the lack of spatial coincidence between seismic
324 and IPR profiles, kriging-based two-dimensional interpolation (Isaaks and Srivastava, 1989) was applied to the IPR dataset to
325 estimate the ice thickness at seismic line locations. The uncertainties associated with the IPR and seismic datasets are ± 20.98
326 m and ± 5.27 m, respectively, resulting in a combined uncertainty of ± 24.05 m. The root mean square error (RMSE) between
327 the two datasets is calculated as ± 29.4 m, exceeding this expected uncertainty range. This discrepancy is attributed primarily
328 to smoothing effects introduced by interpolation in the IPR data, particularly between 1.7 and 2.6 km along line 21YY, within
329 the light blue shaded area in Fig. 10, where seismic data reveal a significantly steeper basal slope. When this localized region
330 is excluded, the RMSE is reduced to ± 24.8 m, approximating the combined uncertainty. Thus, apart from localized artifacts,
331 the seismic and IPR datasets exhibit strong agreement. This consistency supports the mutual reliability of both methods and
332 validates their integrated application for subglacial lake characterization. Despite localized differences, the overall ice
333 thickness estimates from both datasets are in strong agreement, and this cross-validation reinforces the robustness of the
334 seismic interpretation and affirms the consistency between the two geophysical approaches.

335 As additional supporting evidence for this interpretation, a steeply dipping (approximately 52°) bedrock boundary observed
336 along the 21YY line is consistently identified in both the seismic PSTM profile (Figure 9d) and the IPR-derived ice thickness
337 graph (Figure 10), indicating a similar topographic transition in both datasets. This boundary is interpreted as a structural
338 margin delineating the lateral extent of SLD2 and likely functions as a hydrological barrier. The structural congruence observed
339 in both seismic and radar data underscores the effectiveness of integrating these datasets to delineate the boundaries of
340 subglacial lakes, particularly in regions characterized by complex basal topography.

341



342

343 **Figure 10:** A comparison of ice thickness estimates derived from seismic and kriging-interpolated IPR data (Ju et al., 2025) along
 344 the four seismic survey lines reveals high overall consistency between the two datasets, despite localized discrepancies. The light
 345 green shaded region in the 21YY line represents areas where interpolation contributes to the divergence between the two
 346 measurement approaches. The light blue envelope represents the uncertainty bounds associated with the IPR-derived estimates,
 347 while the light red envelope indicates uncertainty bounds for the seismic-derived estimates.

348

349 6 Conclusion

350 Since 2016, the Korea Polar Research Institute (KOPRI) has conducted a series of geophysical investigations to study SLD2
 351 beneath David Glacier, beginning with airborne IPR surveys. In 2021, a seismic survey was carried out to characterize the
 352 internal structure and water column of SLD2. The seismic data revealed strong, laterally continuous reflections with reverse
 353 polarity at the glacier–lake interface, whereas normal-polarity reflections were observed at the glacier–bed and lake–bed
 354 interfaces.

355 A velocity model was constructed on the basis of seismic interpretation, and synthetic seismic data were generated through
 356 wave propagation modeling. A comparison between synthetic and field PSTM sections demonstrated strong agreement in the
 357 timing and polarity of major reflection events at the glacier–lake and lake–bed interfaces, confirming the validity of the velocity
 358 model. This model estimated the ice thickness and lake water column height to be 2250–2300 m and 53–82 m, respectively.
 359 These thickness estimates are in close agreement with independent IPR measurements acquired in 2018 (Ju et al., 2025), further
 360 supporting the reliability of the seismic interpretation.

361 In lines 21Y and 21YY, discontinuous reflections were observed near the glacier base. The discontinuous signals are
 362 interpreted as SLF surfaces formed by basal erosion. Structural alignment across multiple survey lines reveals that these
 363 features are oriented in the direction of ice flow, supporting the interpretation of glacial erosion processes at the bed.

364 This study demonstrates the utility of seismic surveys for the structural characterization of subglacial lake environments. The
365 integrated analysis of seismic and synthetic data provides quantitative constraints on the geometry of SLD2-A beneath David
366 Glacier. This study offers critical insights for future logistical planning, including potential subglacial drilling operations. This
367 study identifies the area within a 1 km radius of S 75.422°, W 155.441° as a suitable candidate site for clean hot-water drilling,
368 given its wide spatial extent, minimum estimated water depth exceeding approximately 50 m, and absence of contamination
369 from surface field camps. The site is therefore considered highly appropriate for future exploration of active subglacial lakes.
370 Furthermore, we plan to conduct follow-up studies incorporating advanced processing techniques such as deghosting,
371 amplitude variation with offset (AVO) analysis, and the development of a refined velocity model that accounts for detailed
372 firn-layer properties. These technical advancements are expected to enhance the resolution and precision of seismic imaging
373 and contribute to a deeper understanding of the subglacial environment.

374 **Data availability**

375 The ICESat-2 data used in this study are available from the National Snow and Ice Data Center (NSIDC). The seismic data
376 and ICESat-2 laser altimetry data used in this study are also available from the Korea Polar Data Center (KPDC) upon request
377 at <https://dx.doi.org/doi:10.22663/KOPRI-KPDC-00001177>. The maps related to Antarctica were created using the
378 Quantarctica dataset version 3.2 (Matsuoka et al., 2018).

379 **Author contributions**

380 HJ: Writing—original draft, investigation, methodology, conceptualization. SGK: Writing—original draft, methodology,
381 conceptualization, supervision. YC: Writing – original draft, data processing, modeling. SP: Data processing methodology.
382 MJL: Writing – original draft. HK: Hot-water drilling. KK: Investigation. YK: Investigation. JIL: Project administration,
383 Funding acquisition.

384 **Competing interests**

385 The authors declare that they have no known competing financial interests or personal relationships that could have appeared
386 to influence the work reported in this paper.

387 **Acknowledgments**

388 We express our sincere gratitude to Sungjun Jeon and the K-route team for their invaluable logistical support. We also extend
389 our appreciation to Do-young Kwon, Jamin Park, Sanghyeok Seo, and Byeongguk Moon for their dedicated assistance in
390 seismic surveys. We name Subglacial Lake D2 Subglacial Lake Cheongsuk (SLC). The name Cheongsuk has a significant

391 meaning, as it is the pen name of Dr. Yeadong Kim, the founder of the KOPRI and former president of the Scientific Committee
392 on Antarctic Research (SCAR). Dr. Kim personally led the IPR and seismic surveys of Subglacial Lake Cheongsuk and
393 coauthored this paper.

394

395 **Financial support**

396 This research was supported by KOPRI grants funded by the Ministry of Oceans and Fisheries (KOPRI project Nos. PE25070).
397

398 **References**

399 Atre, S. R. and Bentley, C. R.: Laterally varying basal conditions beneath ice Streams B and C, West Antarctica,
400 *J. Glaciol.*, 39, 507–514, <https://doi.org/10.3189/s0022143000016403>, 1993.

401 Bell, R. E., Studinger, M., Shuman, C. A., Fahnestock, M. A., and Joughin, I.: Large subglacial lakes in East
402 Antarctica at the onset of fast-flowing ice streams, *Nature*, 445, 904–907,
403 <https://doi.org/10.1038/nature05554>, 2007.

404 Bell, R. E., Ferraccioli, F., Creyts, T. T., Braaten, D., Corr, H., Das, I., Damaske, D., Frearson, N., Jordan, T.,
405 Rose, K., Studinger, M., and Wolovick, M.: Widespread persistent thickening of the east antarctic ice sheet
406 by freezing from the base, *Science*, 331, 1592–1595, <https://doi.org/10.1126/science.1200109>, 2011.

407 Bentley, M. J., Hodgson, D. A., Smith, J. A., Cofaigh, C. Ó., Domack, E. W., Larter, R. D., Roberts, S. J.,
408 Brachfeld, S., Leventer, A., Hjort, C., Hillenbrand, C. D., and Evans, J.: Mechanisms of Holocene
409 paleoenvironmental change in the Antarctic Peninsula region, *Holocene*, 19, 51–69,
410 <https://doi.org/10.1177/0959683608096603>, 2009.

411 Brisbourne, A. M., Smith, A. M., Rivera, A., Zamora, R., Napoleoni, F., Uribe, J. A., and Ortega, M.:
412 Bathymetry and bed conditions of Lago Subglacial CECs, West Antarctica, *J. Glaciol.*, 69, 1–10,
413 <https://doi.org/10.1017/jog.2023.38>, 2023.

414 Christianson, K., Jacobel, R. W., Horgan, H. J., Anandakrishnan, S., and Alley, R. B.: Subglacial Lake Whillans
415 — Ice-penetrating radar and GPS observations of a shallow active reservoir beneath a West Antarctic ice
416 stream, *Earth Planet. Sc. Lett.*, 331–332, 237–245, <https://doi.org/10.1016/j.epsl.2012.03.013>, 2012.

417 Christner, B. C., Priscu, J. C., Achberger, A. M., Barbante, C., Carter, S. P., Christianson, K., Michaud, A. B.,
418 Mikucki, J. A., Mitchell, A. C., Skidmore, M. L., Vick-Majors, T. J., Adkins, W. P., Anandakrishnan, S.,
419 Barcheck, G., Beem, L., Behar, A., Beitch, M., Bolsey, R., Branecky, C., Edwards, R., Fisher, A., Fricker, H.
420 A., Foley, N., Guthrie, B., Hodson, T., Horgan, H., Jacobel, R., Kelley, S., Mankoff, K. D., McBryan, E.,
421 Powell, R., Purcell, A., Sampson, D., Scherer, R., Sherve, J., Siegfried, M., and Tulaczyk, S.: A microbial

422 ecosystem beneath the West Antarctic ice sheet, *Nature*, 512, 310–313, <https://doi.org/10.1038/nature13667>,
423 2014.

424 Dow, C. F., Hubbard, A., Booth, A. D., Doyle, S. H., Gusmeroli, A., and Kulessa, B.: Seismic evidence of
425 mechanically weak sediments underlying Russell Glacier, West Greenland, *Ann. Glaciol.*, 54, 135–141,
426 <https://doi.org/10.3189/2013aog64a032>, 2013.

427 Engelhardt, H., Humphrey, N., Kamb, B., and Fahnestock, M.: Physical conditions at the base of a fast moving
428 Antarctic ice stream, *Science*, 248, 57–59, <https://doi.org/10.1126/science.248.4951.57>, 1990.

429 Filina, I. Y., Blankenship, D. D., Thoma, M., Lukin, V. V., Masolov, V. N., and Sen, M. K.: New 3D bathymetry
430 and sediment distribution in Lake Vostok: implication for pre-glacial origin and numerical modeling of the
431 internal processes within the lake, *Earth Planet. Sc. Lett.*, 276, 106–114,
432 <https://doi.org/10.1016/j.epsl.2008.09.012>, 2008.

433 Frezzotti, M., Tabacco, I. E., and Zirizzotti, A.: Ice discharge of eastern Dome C drainage area, Antarctica,
434 determined from airborne radar survey and satellite image analysis, *J. Glaciol.*, 46, 253–264,
435 <https://doi.org/10.3189/172756500781832855>, 2000.

436 Graves, R. W.: Simulating seismic wave propagation in 3D elastic media using staggered-grid finite differences,
437 *Bulletin of the seismological society of America*, 86, 1091–1106, <https://doi.org/10.1785/BSSA0860041091>,
438 1996.

439 Herron, D. A.: Pitfalls in seismic interpretation: depth migration artifacts, *The Leading Edge*, 19, 1016–1017,
440 <https://doi.org/10.1190/1.1438756>, 2000.

441 Horgan, H. J., Anandakrishnan, S., Jacobel, R. W., Christianson, K., Alley, R. B., Heeszel, D. S., Picotti, S., and
442 Walter, J. I.: Subglacial Lake Whillans — Seismic observations of a shallow active reservoir beneath a West
443 Antarctic ice stream, *Earth Planet. Sc. Lett.*, 331–332, 201–209, <https://doi.org/10.1016/j.epsl.2012.02.023>,
444 2012.

445 Isaaks, E. H. and Srivastava, R. M.: *An Introduction to Applied Geostatistics*, Oxford University Press, Oxford,
446 1989.

447 Johansen, T. A., Ruud, B. E., Bakke, N. E., Riste, P., Johannessen, E. P., and Henningsen, T.: Seismic profiling
448 on Arctic glaciers, *First Break*, 29, 65–71, <https://doi.org/10.3997/1365-2397.20112st1>, 2011.

449 Ju, H., Choi, Y., and Kang, S.-G.: Seismic Survey for the Subglacial Lake in Antarctica. *Geophysics and*
450 *Geophysical Exploration*, 27, 244–257. <https://doi.org/10.7582/gge.2024.27.4.244>, 2024.

451 Ju, H., Kang, S., Han, H., Beem, L. H., Ng, G., Chan, K., Kim, T., Lee, J., Lee, J., Kim, Y., and Pyun, S.:
452 Airborne and Spaceborne Mapping and Analysis of the Subglacial Lake D2 in David Glacier, Terra Nova
453 Bay, Antarctica, *J. Geophys. Res.: Earth Surf.*, 130, <https://doi.org/10.1029/2024jf008142>, 2025.

454 King, E. C., Woodward, J., and Smith, A. M.: Seismic evidence for a water-filled canal in deforming till beneath
455 Rutford Ice Stream, West Antarctica, *Geophys. Res. Lett.*, 31, L20401,
456 <https://doi.org/10.1029/2004gl020379>, 2004.

457 Kirchner, J. F. and Bentley, C. R.: Seismic short-refraction studies on the Ross Ice Shelf, Antarctica, *J. Glaciol.*,
458 24, 313–319, <https://doi.org/10.3189/s0022143000014830>, 1979.

459 Kohnen, H.: The temperature dependence of seismic waves in ice, *J. Glaciol.*, 13, 144–147,
460 <https://doi.org/10.3189/s0022143000023467>, 1974.

461 Krail, P. M. and Shin, Y.: Deconvolution of a directional marine source, *Geophysics*, 55, 1542–1548,
462 <https://doi.org/10.1190/1.1442805>, 1990.

463 Lindzey, L. E., Beem, L. H., Young, D. A., Quartini, E., Blankenship, D. D., Lee, C.-K., Lee, W. S., Lee, J. I.,
464 and Lee, J.: Aerogeophysical characterization of an active subglacial lake system in the David Glacier
465 catchment, Antarctica, *Cryosphere*, 14, 2217–2233, <https://doi.org/10.5194/tc-14-2217-2020>, 2020.

466 Livingstone, S. J., Li, Y., Rutishauser, A., Sanderson, R. J., Winter, K., Mikucki, J. A., Björnsson, H., Bowling, J.
467 S., Chu, W., Dow, C. F., Fricker, H. A., McMillan, M., Ng, F. S. L., Ross, N., Siegert, M. J., Siegfried, M.,
468 and Sole, A. J.: Subglacial lakes and their changing role in a warming climate, *Nature Reviews Earth &*
469 *Environment*, 3, 106–124, <https://doi.org/10.1038/s43017-021-00246-9>, 2022.

470 Matsuoka, K., Skoglund, A., Roth, G., de Pomereu, J., Griffiths, H., Headland, R., Herried, B., Katsumata, K., Le
471 Brocq, A., Licht, K., Morgan, F., Neff, P., Ritz, C., Scheinert, M., Tamura, T., Van de Putte, A., van den
472 Broeke, M., von Deschwanden, A., Deschamps-Berger, C., ... Melvær, Y.: Quantarctica [Dataset].
473 Norwegian Polar Institute. <https://doi.org/10.21334/NPOLAR.2018.8516E961>, 2018.

474 Oliveira, M. S., Henriques, M. V. C., Leite, F. E. A., Corso, G., and Lucena, L. S.: Seismic denoising using
475 curvelet analysis, *Physica A*, 391, 2106–2110, <https://doi.org/10.1016/j.physa.2011.04.009>, 2012.

476 Peters, L. E., Anandakrishnan, S., Alley, R. B., and Smith, A. M.: Extensive storage of basal meltwater in the
477 onset region of a major West Antarctic ice stream, *Geology*, 35, 251–254, <https://doi.org/10.1130/g23222a.1>,
478 2007.

479 Picotti, S., Vuan, A., Carcione, J. M., Horgan, H. J., and Anandakrishnan, S.: Anisotropy and crystalline fabric of
480 Whillans Ice Stream (West Antarctica) inferred from multicomponent seismic data, *J. Geophys. Res. Sol.*
481 *Ea.*, 120, 4237–4262, <https://doi.org/10.1002/2014jb011591>, 2015.

482 Priscu, J. C. and Christner, B. C.: Earth's icy biosphere, in: *Microbial Diversity and Bioprospecting*, edited by:
483 Bull, A. T., ASM Press, Washington, D.C, 130–145, <https://doi.org/10.1128/9781555817770.ch13>, 2003.

484 Qin, L., Qiu, H., Nakata, N., Booth, A., Zhang, Z., Karplus, M., McKeague, J., Clark, R., and Kaip, G.: High-
485 resolution characterization of the firn layer near the West Antarctic ice sheet divide camp with active and
486 passive seismic data, *Geophys. Res. Lett.*, 51, e2024GL108933, <https://doi.org/10.1029/2024gl108933>, 2024.

487 Rignot, E., Mouginot, J., Scheuchl, B., van den Broeke, M., van Wessem, M. J., and Morlighem, M.: Four
488 decades of Antarctic Ice Sheet mass balance from 1979-2017, *P. Natl. Acad. Sci. USA*, 116, 1095–1103,
489 <https://doi.org/10.1073/pnas.1812883116>, 2019.

490 Robinson, E. A. and Treitel, S.: Digital Imaging and Deconvolution, Society of Exploration Geophysicists, Tulsa,
491 Okla, 2008.

492 Rose, K. E.: Characteristics of ice flow in Marie Byrd Land, Antarctica, *J. Glaciol.*, 24, 63–75,
493 <https://doi.org/10.3189/s0022143000014659>, 1979.

494 Schlegel, R., Brisbourne, A. M., Smith, A. M., Booth, A. D., Murray, T., King, E. C., and Clark, R. A.:
495 Subglacial bedform and moat initiation beneath Rutford Ice Stream, West Antarctica, *Geomorphology*, 458,
496 109207, <https://doi.org/10.1016/j.geomorph.2024.109207>, 2024.

497 Siegfried, M. R. and Fricker, H. A.: Thirteen years of subglacial lake activity in Antarctica from multi-mission
498 satellite altimetry, *Ann. Glaciol.*, 59, 42–55, <https://doi.org/10.1017/aog.2017.36>, 2018.

499 Smith, A. M., Woodward, J., Ross, N., Bentley, M. J., Hodgson, D. A., Siegert, M. J., and King, E. C.: Evidence
500 for the long-term sedimentary environment in an Antarctic subglacial lake, *Earth Planet. Sc. Lett.*, 504, 139–
501 151, <https://doi.org/10.1016/j.epsl.2018.10.011>, 2018.

502 Smith, B. E., Fricker, H. A., Joughin, I. R., and Tulaczyk, S.: An inventory of active subglacial lakes in
503 Antarctica detected by ICESat (2003–2008), *J. Glaciol.*, 55, 573–595,
504 <https://doi.org/10.3189/002214309789470879>, 2009.

505 Smith, B. E., Fricker, H. A., Gardner, A. S., Medley, B., Nilsson, J., Paolo, F. S., Holschuh, N., Adusumilli, S.,
506 Brunt, K., Csatho, B., Harbeck, K., Markus, T., Neumann, T., Siegfried, M. R., and Zwally, H. J.: Pervasive
507 ice sheet mass loss reflects competing ocean and atmosphere processes, *Science*, 368, 1239–1242,
508 <https://doi.org/10.1126/science.aaz5845>, 2020.

509 Stearns, L. A., Smith, B. E., and Hamilton, G. S.: Increased flow speed on a large East Antarctic outlet glacier
510 caused by subglacial floods, *Nat. Geosci.*, 1, 827–831, <https://doi.org/10.1038/ngeo356>, 2008.

511 Thoma, M., Grosfeld, K., Smith, A. M., and Mayer, C.: A comment on the Equation of State and the freezing
512 point equation with respect to subglacial lake modelling, *Earth Planet. Sc. Lett.*, 294, 80–84,
513 <https://doi.org/10.1016/j.epsl.2010.03.005>, 2010.

514 Tulaczyk, S., Mikucki, J. A., Siegfried, M. R., Priscu, J. C., Barchek, C. G., Beem, L. H., Behar, A., Burnett, J.,
515 Christner, B. C., Fisher, A. T., Fricker, H. A., Mankoff, K. D., Powell, R. D., Rack, F., Sampson, D.,
516 Scherer, R. P., and Schwartz, S. Y.: WISSARD at Subglacial Lake Whillans, West Antarctica: scientific
517 operations and initial observations, *Ann. Glaciol.*, 55, 51–58, <https://doi.org/10.3189/2014aog65a009>, 2014.

518 Voigt, D. E., Peters, L. E., and Anandakrishnan, S.: ‘Georods’: the development of a four-element geophone for
519 improved seismic imaging of glaciers and ice sheets, *Ann. Glaciol.*, 54, 142–148,
520 <https://doi.org/10.3189/2013aog64a432>, 2013.

521 Wingham, D. J., Siegert, M. J., Shepherd, A., and Muir, A. S.: Rapid discharge connects Antarctic subglacial
522 lakes, *Nature*, 440, 1033–1036, <https://doi.org/10.1038/nature04660>, 2006.

523 Winsborrow, M. C. M., Clark, C. D., and Stokes, C. R.: What controls the location of ice streams?, *Earth-Sci.
524 Rev.*, 103, 45–59, <https://doi.org/10.1016/j.earscirev.2010.07.003>, 2010.

525 Woodward, J., Smith, A. M., Ross, N., Thoma, M., Corr, H. F. J., King, E. C., King, M. A., Grosfeld, K., Tranter,
526 M., and Siegert, M. J.: Location for direct access to subglacial Lake Ellsworth: an assessment of geophysical
527 data and modeling, *Geophys. Res. Lett.*, 37, L11501, <https://doi.org/10.1029/2010gl042884>, 2010.

528 Wright, A. and Siegert, M.: A fourth inventory of Antarctic subglacial lakes, *Antarct. Sci.*, 24, 659–664,
529 <https://doi.org/10.1017/s095410201200048x>, 2012.

530 Yan, S., Blankenship, D. D., Greenbaum, J. S., Young, D. A., Li, L., Rutishauser, A., Guo, J., Roberts, J. L., van
531 Ommen, T. D., Siegert, M. J., and Sun, B.: A newly discovered subglacial lake in East Antarctica likely
532 hosts a valuable sedimentary record of ice and climate change, *Geology*, 50, 949–953,
533 <https://doi.org/10.1130/g50009.1>, 2022.

534 Yilmaz, Ö.: *Seismic Data Analysis: Processing, Inversion, and Interpretation of Seismic Data*, Society of
535 Exploration Geophysicists, Tulsa, Okla, 2001.

536 Zechmann, J. M., Booth, A. D., Truffer, M., Gusmeroli, A., Amundson, J. M., and Larsen, C. F.: Active seismic
537 studies in valley glacier settings: strategies and limitations, *J. Glaciol.*, 64, 796–810,
538 <https://doi.org/10.1017/jog.2018.69>, 2018.